

Photoinduced twist and untwist of moiré superlattices in TMDC heterobilayers

C. J. R. Duncan^{1,2}, A. C. Johnson³, I. Maity^{4,5}, A. Rubio⁵, M. Gordon¹, A. C. Bartnik¹, M Kaemingk^{1,6}, W. H. Li^{1,7}, M. B. Andorf¹, C. A. Pennington^{1,8}, I. V. Bazarov¹, M. W. Tate⁹, D. A. Muller^{10,11}, J. Thom-Levy¹², S. M. Gruner^{9,11}, A . M. Lindenberg¹³, F. Liu^{★3}, and J. M. Maxson^{★1}

¹Cornell Laboratory for Accelerator-Based Sciences and Education, Cornell University, Ithaca, NY, USA

²SLAC National Accelerator Laboratory, Menlo Park, CA, USA

³Department of Chemistry, Stanford University, Stanford, CA, USA

⁴Newcastle University, Newcastle, UK

⁵Max Planck Institute for the Structure and Dynamics of Matter, Hamburg, Germany

⁶Los Alamos National Laboratory, Los Alamos, NM, USA

⁷Brookhaven National Laboratory, Upton, NY, USA

⁸University of California Los Angeles, Los Angeles, CA, USA

⁹Laboratory of Atomic and Solid State Physics, Cornell University, Ithaca, NY, USA

¹⁰School of Applied and Engineering Physics, Cornell University, Ithaca, NY, USA

¹¹Kavli Institute at Cornell for Nanoscale Science, Cornell University, Ithaca, NY, USA

¹²Laboratory for Elementary-Particle Physics, Cornell University, Ithaca, NY, USA

¹³Department of Materials Science and Engineering, Stanford University, Stanford, CA, USA

★ *Corresponding authors:* fliu10@stanford.edu, jmm586@cornell.edu

Abstract

Two-dimensional twisted bilayer moiré structures provide a versatile material platform for realizing a rich variety of strongly correlated electronic quantum phases intricately coupled with the periodically modulated lattice structures. In this work, we use ultrafast electron diffraction to directly reveal the photoinduced dynamic evolution of the moiré superlattice in 2° and 57° twisted $\text{WSe}_2/\text{MoSe}_2$ heterobilayers. Upon above-band-gap photoexcitation, the moiré superlattice diffraction features are enhanced within 1 ps and subsequently suppressed several picoseconds after, accompanied by a collective lattice excitation of a moiré phonon mode with sub-THz frequency. This unique response deviates markedly from typical photoinduced lattice heating, and suggests dynamic twisting and untwisting of the local moiré chiral structure. We infer large oscillations in the local twist angle, approaching 1° peak to trough, that are driven by ultrafast charge carrier excitation and relaxation — a phenomenon further supported by molecular dynamics simulations. Our findings suggest a novel approach for real-time dynamic reconfiguration of moiré superlattices to achieve ultrafast modulation of their strongly correlated behaviors.

1 Introduction

Since the discovery of superconductivity and correlated insulating states in twisted bilayer graphene (TBG) [1, 2, 3, 4], moiré structures from twisted bilayers have emerged as versatile platforms for exploring a wide range of strongly correlated quantum phases. Compared with TBG, transition metal dichalcogenide (TMDC) moiré structures exhibit higher effective mass and more robust couplings [5, 6, 7], presenting promising opportunities for the manipulation and design of additional quantum phenomena such as correlated insulators [8, 9], fractional quantum anomalous Hall effects [10], and generalized Wigner crystals [11, 12, 13]. Many of these strongly correlated quantum phases stem from the reduced screening and strong Coulomb interaction of electrons in two-dimensional geometry, dominating over the significantly lowered kinetic energy in the flat moiré minibands [14]. The band structure, magnetism, and superconducting properties can be readily tuned with twist angles and band fillings, which are strongly affected by the interplay between the moiré superlattice morphology and the electronic potentials [15, 16, 17, 18, 19].

Due to the periodic variation of atomic overlap, the mesoscale moiré lattice structure often undergoes picometer-scale relaxation and deformation, a phenomenon known as periodic lattice distortion (PLD). The reconstructed structures foster the formation of localized states and additional flat bands, deepen the moiré potential [20, 21], and enhance electron-phonon couplings significantly [22]. In magic angle twisted bilayer graphene, strong electron-phonon coupling has been proposed as a key factor affecting correlated insulator behavior and phonon-mediated superconductivity [23]. Furthermore, TMDC monolayers and bilayers feature long-lived intralayer and interlayer excitons with spin-valley polarizations [24, 25], which can be confined in the periodic trap potentials of moiré

structures, demonstrating additional excitonic flat minibands [26, 27, 28, 29, 30], with strong exciton–phonon interaction [31]. In TMDC moiré superlattices, charge carriers are theorized to form small polarons similar to a charge-density-wave state, in which the motion of the lattice in reaction to exciton formation enhances the spatial modulation of the exciton wave-function [32, 33, 34, 35]. Visualizing the dynamical lattice responses to light and charge carrier excitation can be of key importance for understanding the electron-phonon coupling in a moiré system. Furthermore, if the moiré superlattice structure can be dynamically tuned on ultrafast timescales, it will open up unique opportunities to modulate the corresponding quantum phases of matter through their close interplay with the superlattice twist angles and potentials.

Despite considerable theoretical progress and growing interest, direct experimental investigation of the photoinduced lattice dynamics in moiré structures remains limited. The majority of the experimental work to date has relied on optical probes, such as photoluminescence [29], and transient absorption/reflection spectroscopy [36, 32], which are not directly sensitive to lattice motions. In contrast, ultrafast electron diffraction (UED) is the ideal direct experimental tool for precise characterization of the transient lattice structural dynamics. However, the application of UED to twisted bilayer moiré structures has been held back by significant challenges due to the small diffraction volume and the microscopic size of the high quality twisted bilayers, and the stringent brightness requirements for the pulsed electron probe necessary to resolve fine details in the momentum space of the moiré mini-Brillouin zone.

In this work, we carried out UED measurements on twisted $\text{WSe}_2/\text{MoSe}_2$ moiré structures, taking advantage of deterministic large-area TMDC monolayer exfoliation and assembly [37], together with the unique electron beam collimation and lensing design [38]. We have identified key electron diffraction features from the moiré superlattices, appearing as satellite peaks dressing the main Bragg peaks. The time-dependent modulation of the satellite diffraction peaks provides precise evidence of the real-time evolution of the moiré structures upon photoexcitation. Our UED results demonstrate that the local twist angle dynamically evolves as the interlayer separation changes upon carrier injection, consistent with the prediction that the twist-angle and interlayer separation are intertwined [39]. Associated with exciton formation and localization, we also directly identify a photoinduced transverse and coherent sub-THz torsional motion with the same spatial periodicity as the moiré superlattice, in agreement with the predictions of our driven-oscillator model. The results will open the door to coherent optical control of the moiré structures as a means of manipulating their associated excitonic and strongly-correlated collective electronic behaviors [32, 40, 41, 42, 43].

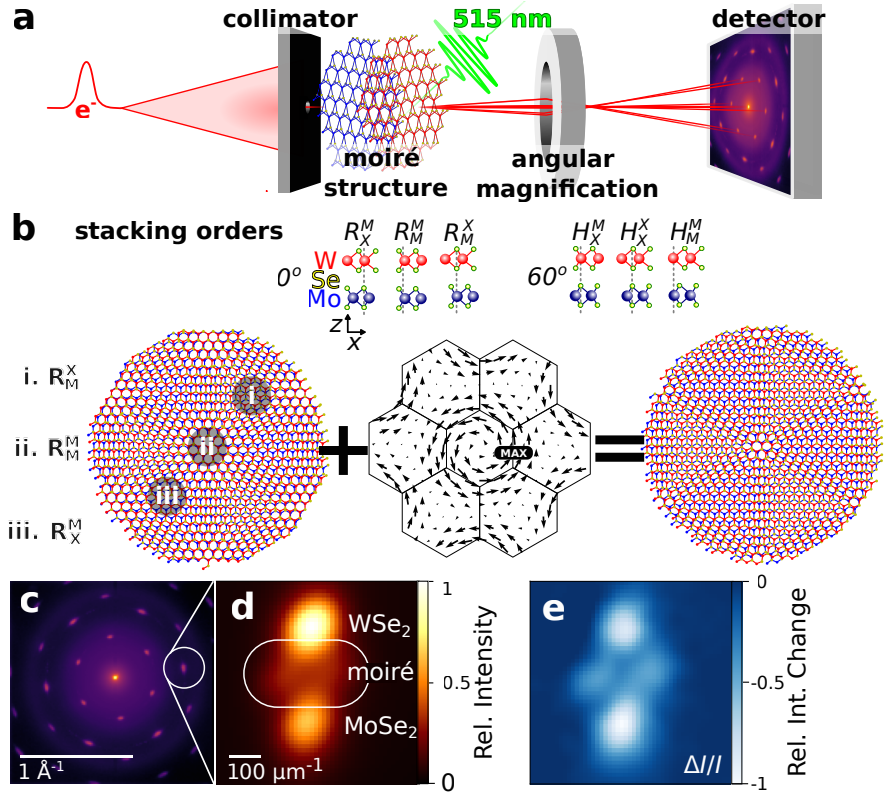


Figure 1: Experimental scheme and representative diffraction images. (a) Schematics of the UED setup. (b) Schematics of PLD in a bilayer moiré structure consisting of alternating domains with different stacking orders. PLD expands the size of energetically favorable stacking domains. (c) Wide-angle view of scattering patterns from 2° WSe₂/MoSe₂ heterobilayers. (d) Zoom on the (2,-1) diffraction peak at high angular magnification. (e) Photoinduced changes of scattering intensity, highlighting the strong response of the moiré satellite peaks. The difference is obtained by subtracting the diffraction pattern at 4 ps after photoexcitation from the static diffraction pattern in panel (d).

2 Results: observation of photoinduced moiré superlattice motion

The schematic of the UED setup is shown in Fig. 1(a), and described in detail in the Methods section. Our electron beam collimation and lensing system are capable of resolving diffraction features down to $100 \mu\text{m}^{-1}$ [44, 38], making it particularly effective for resolving the moiré mini Brillouin zone. The high-quality, large-area $\text{WSe}_2/\text{MoSe}_2$ moiré structures with twist angles of 2° and 57° are constructed by stacking macroscopic monolayers from gold tape exfoliation [37, 45]. Figure 1(c) and (d) represent typical diffraction patterns from the large area 2° twisted $\text{WSe}_2/\text{MoSe}_2$ moiré structure. The twist angles are measured between the monolayer Bragg peaks in the electron diffraction pattern, and confirmed with second harmonic generation, as shown in the Extended Data.

With only threefold rotational symmetry, TMDC bilayers can exhibit different stacking orders locally, categorized as rhombohedral R type (for small twist angles) or hexagonal H type (for twist angles close to 60°). Due to variations in atomic overlaps at different local stacking configurations, the bilayer moiré superlattice will relax to optimize lower-energy stacking orders, and PLD occurs. This leads to a small additional adjustment of the local twist angle at alternating stacking domains [46], as illustrated in Figure Fig. 1(b). Consequently, electron diffraction from the moiré lattice is not merely a superimposition of the monolayer Bragg peaks. Instead, the diffraction patterns exhibit additional satellite peaks, in accordance with the superlattice Brillouin zone folding in both electron and phonon dispersion [46, 47, 48, 49]. The intensity of these satellite peaks is directly correlated with the strength of the periodic lattice strain [49]. A detailed quantitative description of this relationship, derived from kinematic diffraction theory, is provided in the Supplemental Information.

To resolve the moiré satellite peaks, we magnify the feature at index (2,-1) highlighted in Fig. 1(c) with post-sample projection optics. The magnified view clearly captures both the Bragg peaks of the individual monolayers and the two satellite peaks of the moiré structure, as demonstrated in Figs. 1 (d). The intensity of the satellite peaks, located between the Bragg peaks, is maximally enhanced due to constructive interference between the scattering amplitudes of the individual monolayers. This constructive interference arises from the fact that the PLDs in the top and bottom layers have equal magnitude and are anti-parallel [15, 49].

Upon excitation with a 515 nm pump laser, the satellite peaks exhibit a more pronounced response relative to the main Bragg peaks, significantly enhancing the contrast, as shown in Fig. 1(e), suggesting that the dynamic atomic interactions within the twisted bilayer systems are distinct from individual monolayers.

The picosecond time-domain changes of the Bragg peak intensity and the moiré superlattice satellite peak intensities for the $2^\circ \text{WSe}_2/\text{MoSe}_2$ and $57^\circ \text{WSe}_2/\text{MoSe}_2$ samples are shown in Fig. 2(a)(b)(d)(e). Upon photoexcitation, the intensities

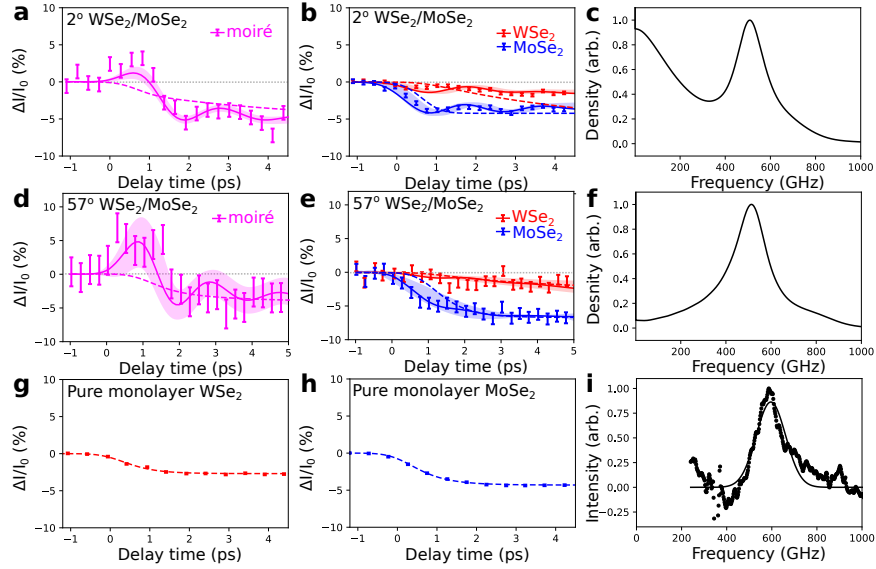


Figure 2: Time dependent changes of the UED intensities. UED photoexcitation is fixed at 515 nm. Error bars show Poisson uncertainties. Solid lines are fits produced by the dynamical model in Eq.(1) and the shaded area is the 95% confidence interval. The dashed line is the prediction from lattice heating alone. (a), (b) Normalized diffraction intensity changes of superlattice peaks and individual monolayer Bragg peaks for 2° WSe₂/MoSe₂ moiré structure. (d), (e) Normalized intensity changes of 57° WSe₂/MoSe₂ moiré structure. (g), (h) Normalized intensity changes of isolated monolayers measured under an identical excitation scheme. (c), (f) Power spectral density of the model for the 2° and 57° WSe₂/MoSe₂ moiré structures. (i) Low-frequency Raman spectroscopy of 2° WSe₂/MoSe₂ moiré structure.

of the main Bragg peaks decrease for both twisted bilayers and isolated monolayers. Typically, photoexcitation enhances the thermal motion of the lattice, which leads to a reduction in diffraction intensity due to the Debye-Waller (DW) effect. Similar photoinduced reductions in UED intensities and lattice heating have been reported in other 2D systems including monolayers and bilayers at higher twist angles [50, 51, 52, 53].

In stark contrast to the typical DW effect, the satellite peak intensities exhibit a pronounced rise within the first picosecond after photoexcitation, as shown in both Fig. 2(a) and (c). Unlike the reduction of the main Bragg peak intensities, this anomalous response of the satellite peaks provides compelling evidence of distinct lattice motion on the moiré length scale that differs significantly from mere thermal excitation. When we only consider the exponential suppression of diffraction intensity due to incoherent lattice motions (represented by the DW factor), the resulting best fit of the purely thermal model is shown with dashed lines in Figs. 2(a) and (d), and reveals a notable discrepancy with the observed data.

To better explain the data, we introduce a coherent driving force into our model. The microscopic origin of the driving force is the mutual attraction between layer-separated photoexcited carriers (electrons and holes). Our model treats the driving force as spatially uniform and out-of-plane, with a time dependence determined by the carrier relaxation time. The out-of-plane driving couples to a cork-screw-like lattice motion via the interplay of elastic and van der Waals (vdW) forces in the moiré structure. The quantitative details of this mechanism are further explored below. Electron diffraction is sensitive only to the in-plane component of this chiral, 3D motion (at our normal incidence angle and 140 keV beam energy). The resulting fits to our UED data are shown with solid lines in Figs. 2(a) and (d), effectively capturing both the overall dynamics and the coherent oscillations observed. Our interpretation is complementary to all-optical pump-probe measurements on twisted $\text{WSe}_2/\text{MoSe}_2$, published by others, that show in transient reflectivity data the signature of sub-terahertz out-of-plane breathing following pump excitation above the band gaps of both layers [54].

The corresponding frequency-domain responses, as presented in Fig. 2 (c) and (f), reveal a predominant mode near 0.5 THz. This dominant mode matches well with the low-frequency Raman spectroscopy measurements performed on the same samples, shown in Fig. 2(i). This frequency corresponds to the interlayer shear motions, consistent with the frequency reported for $\text{MoSe}_2/\text{WSe}_2$ twisted bilayers previously [55]. This frequency is not observed in pure monolayers on the same Si_3N_4 substrate, therefore, it is not likely the acoustic breathing mode from the sound-wave-round-trip time in the substrate [56].

Elaborating on the details of our model, we combine coherent and thermal effects by first simulating the deterministic motion of a zero-temperature lattice in response to the driving force, and then multiplying the predicted diffraction intensity with a DW-type exponentially decaying envelope. The simulation treats

the displacement of each atom from its initial position in the WSe₂/MoSe₂ moiré structures as a driven system of coupled linear ordinary differential equations. Indexing the coordinate axis (x, y, z) as $(0, 1, 2)$ and writing the j th vector component of the displacement of the i th atom x_{ij} , the system of equations can be expressed:

$$\ddot{x}_{ij} = F_{ij}(t) - \sum_{k\ell q} U_{kij} U_{k\ell q} \sqrt{\frac{m_\ell}{m_i}} (2\omega_k \dot{x}_{\ell q} + \omega_k^2 x_{\ell q}). \quad (1)$$

Here, ω_i represents the normal mode frequencies of lattice oscillation and m_i the mass of the i th atom. The tensor U_{kij} is the displacement of the i th atom along the j th axis when the k th normal mode is excited, normalized such that, for all k , $\sum_{\ell q} U_{k\ell q}^2 = 1$. The inclusion of a driving term in Eq. (1) is equivalent to a time-dependent change in the location of the potential energy minima of each atom [57]: a short derivation of the equivalent formulation can be found in the Supplemental Information.

For the driving term $F_{ij}(t)$, we choose the functional form,

$$F_{i0}(t) := F_{i1}(t) := 0 \quad (2)$$

$$F_{i2}(t) := m_i^{-1} L_i \left[a e^{-t/\tau_a} + b \left(1 - e^{-t/\tau_b} \right) \right] H(t), \quad (3)$$

where m_i is the mass of the i th atom and L_i indicates whether the atom belongs to the WSe₂ layer ($L_i = 1$) or the MoSe₂ ($L_i = -1$). This functional form can be thought of as the leading term in a more general Fourier expansion of the local variation in excited carrier density and electron-phonon coupling across the moiré supercell. The leading term must be uniform and out-of-plane because of the c_3 rotational symmetry of the lattice [57], which is not broken when free carriers are photoexcited. The factor L_i ensures that the layers are driven in opposite directions and is motivated by the physical mechanisms of interlayer attraction and thermal expansion, discussed further below. H is the Heaviside step function, and a, b are the fit parameters describing the initial and final strength the force, with τ_a, τ_b relaxation times. We set τ_b equal to the independently measured 1 ps timescale of carrier relaxation, and $\tau_a = \tau_b/2$ due the quadratic dependence on charge of the initially attractive force, as further described in the Discussion section. The model assumes that at acoustic frequencies the lattice is critically damped due to irreversible transfer of energy to the Si₃N₄ substrate. Normal modes of oscillation are found from molecular dynamics simulations, with potentials fit to agree with density-functional-theory calculations in the neighborhood of each atom [58, 59, 60, 61].

We quantify the explanatory power of our coherent-driving model relative to the basic DW thermal model through statistical analysis [62], summarized in the Methods section and elaborated in the Supplementary Information. Based on our UED data, and assuming normally distributed residuals, we find a probability $p < 10^{-3}$ that there is no contribution from a coherent driving force.

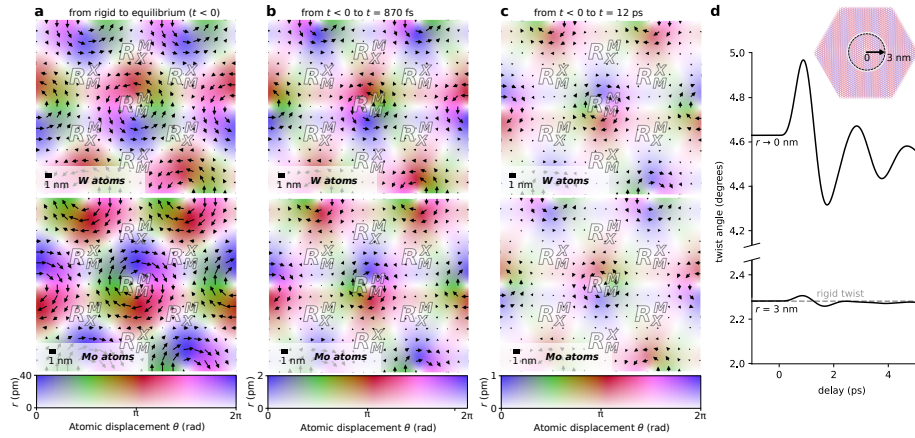


Figure 3: Twisting of the 2° $\text{WSe}_2/\text{MoSe}_2$ lattice versus time, extracted from our dynamical model fitted to UED experimental data. (a) At equilibrium, atoms are displaced from sites of the unphysical, rigidly rotated lattice by vdW forces. Hue shows displacement direction, saturation displacement magnitude. (b) Snapshot of the transverse displacement of atoms from equilibrium at 870 fs after photoexcitation, dominated by torsion about the R_M^M stacking domain center. (c) Snapshot at 12 ps following photoexcitation, i.e., after the decay of the oscillatory transient, showing the untwisting of the equilibrium reconstruction. (d) Fitted atomic displacement as a function of radial distance from the vortex center, expressed as a twist angle. A similar figure for the 57° case is included in the Extended Data.

Taking the solution to Eq. (1) that best fits our UED data, we are able to infer the displacement of W, Mo and Se atoms from their initial positions at different delay times. The corresponding real-space snapshots of the 2° twisted bilayers are shown in Fig. 3. Upon photoexcitation, a torsional vortex appears in the moiré supercell, reflecting the dynamical twisting and untwisting of the moiré structure. To quantify these effects, we evaluate the change in local twist angle with delay time under the small angle approximation,

$$\theta_{\text{local}} = \frac{1}{\|\mathbf{r}\|^2} (\|\delta\mathbf{x}_W \times \mathbf{r}\| - \|\delta\mathbf{x}_{\text{Mo}} \times \mathbf{r}\|), \quad (4)$$

where $\delta\mathbf{x}_X(\mathbf{r})$ is the displacement of atomic species X , and \mathbf{r} is the position vector taken from the vortex center. To smooth discrete atomic coordinates, a fifth-order polynomial is fit to the expression in parentheses. The limit $\mathbf{r} \rightarrow 0$ of Eq. (4) is well-defined and gives the best summary of the local atomic environment.

Figure 3 (b) shows that a short time (~ 800 fs) following photoexcitation, each moiré supercell contains a prominent vortex centered on the R_M^M domain. Comparison with Fig. 3 (a) reveals that this movement reinforces the PLD of the original moiré structures. By contrast, at the late delay time shown in Fig. 3 (c) the twist has reversed sign relative to the PLD present in the relaxed moiré structure. This behavior of the local twist angles is mapped to the coarse-grained features observed in the experimental data: the transient increase in the satellite peak intensity corresponds to the reinforcement of the moiré PLD at earlier times, while the suppression of the satellite peak intensity at later times corresponds to the untwisting that weakens the PLD. The evolution of the 57° sample is qualitatively similar and presented in the Extended Data.

The agreement between our experimental data and the model summarized in Eq. (1) depends essentially on the coupling between in-plane and out-of-plane lattice degrees of freedom. The microscopically accurate form of Eq. (1) obscures this fact. To better elucidate the coupling mechanism, it is helpful to refer to a toy model that retains only two mesoscopic degrees of freedom: the twist angle θ about the vortex center in the moiré supercell and the spatially averaged interlayer separation z . The quadratic Lagrangian L in these variables is reproduced in the Supplementary Information: previously published work on moiré PLD by others has proposed essentially the same picture [49, 46]. The only addition we make is the mixing term — a correction implied by the Kolmogorov-Crespi (KC) intermolecular potential that governs the microscopic lattice dynamics (an expression for the KC potential is provided in the Methods section) [63]. At our 2° and 3° twist angles, the in-plane elastic restoring force acting on θ is stronger than the out-of-plane vdW force acting on z , so that when the system is decoupled θ oscillates at a higher frequency than z . The hybridization that results from a mixing term in a two-variable, quadratic Lagrangian is straightforward to compute: the lower frequency hybrid mode is mostly out of plane motion and the higher frequency mode mostly in plane motion. The out-of-plane driving force excites predominantly the former motion, which has

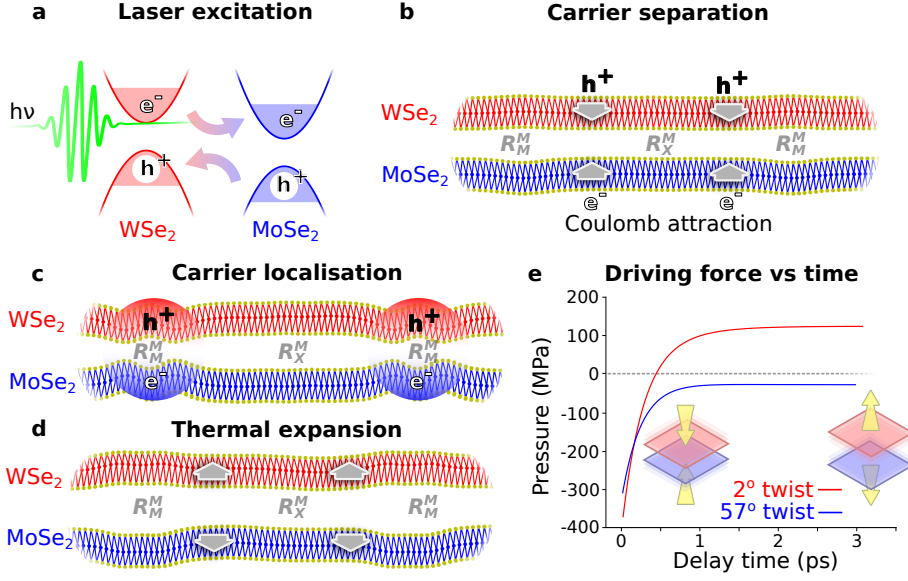


Figure 4: Charge transfer mechanism driving the lattice response: (a) 515 nm pump photons promote charges into the conduction band; type-II band misalignment causes negative carriers to move to the MoSe₂ layer and positive to WSe₂. (b)-(c) Coulomb forces from layer-separated charges pull the layers together. Simulated atomic displacements from equilibrium are exaggerated in the figure by a factor 100. (d)-(e) Carrier relaxation causes the lattice to heat; thus, the driving force applied to the lattice evolves from compressive at early delay times to expansive at late delay times. (e) The best-fit driving force that results in the solid curves shown in Fig. 2.

a longer lifetime because it is lower frequency. Inspection of the microscopically accurate simulation results presented in Fig. 3 tells the same story as the toy model.

3 Discussion: Origin of the twist and untwist of moiré structures locally

In this section, we posit a physical interpretation of Eq. (3), the biexponential ansatz for the forces driving lattice motion. The fitted dependence of out-of-plane pressure on time is shown in Fig. 4(e). Due to the type-II band alignment in TMDC bilayers such as WSe₂/MoSe₂, photoexcitation leads to ultrafast interlayer charge transfer, occurring within 100 fs, as illustrated in Fig. 4(b)-(c) [64, 65, 66, 50, 51, 67]. The electrons tend to reside on the MoSe₂ layer with lower conduction band (CB) minimum energies, while holes tend to reside on

the WSe₂ layer with higher valence band (VB) energies. Such effects lead to opposite charges accumulating across the bilayer vdW interface, resulting in attractive Coulomb interactions between the layers. From our incident fluence and sample absorptivity [54], we estimate an initial carrier density of $9 \times 10^{13} \text{ cm}^{-2}$. This initial carrier density is above the Mott threshold, leading to the formation of an electron-hole plasma with layer-separated opposite charges [68]. As a result, the early time dynamics can be well-modeled simply using the interlayer Coulomb attraction with a uniform distribution of charge carriers, treated as a charged parallel plate capacitor pulled together by a pressure P :

$$P = -e^2 n^2 / \epsilon, \quad (5)$$

with n the surface number density of charge-hole pairs and $\epsilon = 7.5$ the dielectric permittivity of the bilayer [69, 68]. The capacitor model implies that the carrier density excited by our pump laser corresponds to a pressure of 0.3 GPa, which is consistent with the pressures estimated from our UED data (0.4 GPa for 2° WSe₂/MoSe₂ and 0.3 GPa for 57° WSe₂/MoSe₂). The quadratic dependence in Eq. (5) implies that this component of the driving force decays twice as fast as the carrier population.

After a few ps following initial excitation, the cooling and decay of charge carriers efficiently reduces the population of electrons and holes. The population decay of charge carriers is fast, a picture that is validated by a complementary time-resolved angle-resolved photoemission spectroscopy (trARPES) measurement included in the Extended Data, carried out under similar wavelength, fluences, and temperature, on a separate 3° twisted MoSe₂/WSe₂ heterobilayer. The trARPES results demonstrate that K point electrons decay with a time constant of 0.6 ps while the VB holes at the K point exhibit biexponential decay with a fast ~ 2 ps component and a slower > 5 ps component. The fast decay of K point electrons is due to the relaxation to the CB minimum at the Q point, which is located outside the field of view in our UED data [70]. On the other hand, the VB maximum is located at the K point.[70] Therefore, the K point holes may represent the majority of the hole concentration in MoSe₂/WSe₂ heterobilayer. The fast decay is a clear indication of efficient carrier-carrier scattering and recombination under room temperature.

From the decay dynamics, we can estimate that the charge carrier density approaches the Mott threshold at 3-4 ps following photoexcitation. At this time, electrons and holes begin to bind into interlayer excitons. Soon after, as the carrier density decays to a similar order of magnitude as the density of moire cells ($1 \times 10^{12} \text{ cm}^{-2}$ for 2° WSe₂/MoSe₂ and $2.5 \times 10^{12} \text{ cm}^{-2}$ for 3° WSe₂/MoSe₂), the excitons become trapped at the local minima of the moire potential energy surface. Exciton trapping occurs at R_M^M and H_X^M sites of the moiré supercell (see Fig. 1(b), (c)) due to the more efficient interlayer orbital overlaps and lower trap energy [71, 72, 73]. The pinching force from trapped excitons scales linearly in charge density and is thus weaker but longer lived than the capacitive force. As discussed further in the Supplementary Information, experimentally

discriminating this subleading contribution to lattice motion requires higher signal to noise at longer delay times, which is challenging to achieve with the exceptionally fine diffraction resolution that is required to resolve the satellite peaks - better than $100 \mu\text{m}^{-1}$. The ability to measure the lattice response at multiple carrier-density scales in the same dataset would provide an even richer empirical picture of the physics at play, which is a strong motivation for further instrument development to improve signal to noise.

The equilibration of photoexcited carriers with the lattice leads to expansive pressure (negative-sign in our convention), which is provided by anharmonic coupling to a rising population of optical phonons. Using the thermal expansion coefficient typical of monolayer TMDs, on the order 10^{-5} [74, 54], an applied pressure of between 100 MPa and 1 GPa corresponds to a temperature increase on the order of tens of Kelvin, which is consistent with the scale of the energy we inject into the system with our single mJ/cm^2 pump fluence.

Adding a caveat to the role we assign to charge transfer, earlier published terahertz spectroscopy measurements suggest that the charge transfer process can saturate as the stored energy per particle approaches the band misalignment [75]. Hence, Eq. (5) is best understood as valid in the low fluence limit. Typically, signal to noise in UED requires pumping samples at single or multiple mJ/cm^2 , which can push the system into a non-perturbative regime that is challenging to model or simulate. More generally, even without charge transfer, excited carriers can couple to the moiré length-scale lattice motion: however, the large size of the moiré supercell (10^3 atoms) creates difficulties when applying the standard ab initio deformation potential approach to calculating these effects [76].

The model summarized in Eq. (1) assumes that the dielectric properties of $\text{WSe}_2/\text{MoSe}_2$ are unchanged by photoexcitation, but at the next to leading order of approximation, photoinduced changes to the dielectric response can also play a role. Published x-ray scattering data on multilayer MoSe_2 shows out-of-plane oscillations following photoexcitation [56]. Unlike the heterobilayer we consider in this work, in homogenous MoSe_2 there is no mechanism for interlayer charge transfer. The proposal is instead that the screening effect of photoexcited free carriers changes the quantum-zero-point energy associated with fluctuating dipole moments, producing a Casimir force. This Casimir force is proportional to $n^{1/2}$ (here again n is the photoexcited charge density). Applying this model to our experiment, we compute a pressure on the order of 10 MPa, much less than the pressures implied by the fit of Eq. (1) to our UED data.

4 Outlook

Our UED experiment characterizes the nonequilibrium motion of TMDC moiré superlattices upon photoexcitation. We reveal local dynamic twisting and untwisting within moiré super cells, driven by excitation, transfer, and relaxation

of charge carriers and lattice heating, in accord with the recent theoretical predictions on the strong-coupling between twist-angle and interlayer separation in twisted bilayers [39]. Our UED measurements provides direct experimental evidence of transverse, coherent lattice motion in moiré structures. This result compliments recent carrier dynamic measurements in twisted TMDC moire structures revealed with all-optical pump-probe measurements [54], and time-resolved angle-resolved photoemission spectroscopy (trARPES) [72, 71]. The local changes of lattice deformation in the moiré unit cell demonstrate the possibility to dynamically modulate the moire potentials in real time. Our results paves the way to coherent ultrafast, nanoscale control of exotic chiral acoustic, excitonic, polaronic and strongly-correlated collective degrees of freedom in bilayer TMDCs, and the experimental and modeling techniques we demonstrate here are equally applicable to a variety of fascinating quasi-2D systems [32, 40, 41, 42, 43].

In our model, the driving force for the local expansion and contraction are purely out-of-plane, which couples strongly with in-plane components [39]. Reducing the interlayer distance increases the out-of-plane vdW interaction [63, 46, 77], causing atoms to shift in plane to a new mechanical equilibrium. The directional in-plane twist motion reinforces or disrupts the torsional displacement in a moiré structure. This local lattice motion from ultrafast contraction is intrinsically chiral [78, 42]. Such ultrafast lattice motion might generate ultrafast effective magnetic fields that loop around stacking-domain boundaries, analogous to effects demonstrated for chiral phonons [79, 80, 81, 42]. Based on numerical estimates of the static, out-of-plane polarization in the heterobilayer [82], transient magnetic field strengths could be as high as 10 gauss, providing the potential for realizing ultrafast chiral-motion induced magnetism on a 2D material platform.

References

- [1] Cao, Y., Fatemi, V., Demir, A., Fang, S., Tomarken, S.L., Luo, J.Y., Sanchez-Yamagishi, J.D., Watanabe, K., Taniguchi, T., Kaxiras, E., *et al.*: Correlated insulator behaviour at half-filling in magic-angle graphene superlattices. *Nature* **556**(7699), 80–84 (2018)
- [2] Cao, Y., Fatemi, V., Fang, S., Watanabe, K., Taniguchi, T., Kaxiras, E., Jarillo-Herrero, P.: Unconventional superconductivity in magic-angle graphene superlattices. *Nature* **556**(7699), 43–50 (2018)
- [3] Yankowitz, M., Chen, S., Polshyn, H., Zhang, Y., Watanabe, K., Taniguchi, T., Graf, D., Young, A.F., Dean, C.R.: Tuning superconductivity in twisted bilayer graphene. *Science* **363**(6431), 1059–1064 (2019)
- [4] Lu, X., Stepanov, P., Yang, W., Xie, M., Aamir, M.A., Das, I., Urgell, C., Watanabe, K., Taniguchi, T., Zhang, G., *et al.*: Superconductors, or-

- bital magnets and correlated states in magic-angle bilayer graphene. *Nature* **574**(7780), 653–657 (2019)
- [5] Miao, S., Wang, T., Huang, X., Chen, D., Lian, Z., Wang, C., Blei, M., Taniguchi, T., Watanabe, K., Tongay, S., *et al.*: Strong interaction between interlayer excitons and correlated electrons in wse2/ws2 moiré superlattice. *Nature communications* **12**(1), 3608 (2021)
- [6] Huang, X., Wang, T., Miao, S., Wang, C., Li, Z., Lian, Z., Taniguchi, T., Watanabe, K., Okamoto, S., Xiao, D., *et al.*: Correlated insulating states at fractional fillings of the ws2/wse2 moiré lattice. *Nature Physics* **17**(6), 715–719 (2021)
- [7] Wu, F., Lovorn, T., Tutuc, E., MacDonald, A.H.: Hubbard model physics in transition metal dichalcogenide moiré bands. *Physical review letters* **121**(2), 026402 (2018)
- [8] Wang, L., Shih, E.-M., Ghiotto, A., Xian, L., Rhodes, D.A., Tan, C., Claassen, M., Kennes, D.M., Bai, Y., Kim, B., *et al.*: Correlated electronic phases in twisted bilayer transition metal dichalcogenides. *Nature materials* **19**(8), 861–866 (2020)
- [9] Shimazaki, Y., Schwartz, I., Watanabe, K., Taniguchi, T., Kroner, M., Imamoğlu, A.: Strongly correlated electrons and hybrid excitons in a moiré heterostructure. *Nature* **580**(7804), 472–477 (2020)
- [10] Park, H., Cai, J., Anderson, E., Zhang, Y., Zhu, J., Liu, X., Wang, C., Holtzmann, W., Hu, C., Liu, Z., Taniguchi, T., Watanabe, K., Chu, J.-H., Cao, T., Fu, L., Yao, W., Chang, C.-Z., Cobden, D., Xiao, D., Xu, X.: Observation of fractionally quantized anomalous hall effect. *Nature* **622**(7981), 74–79 (2023)
- [11] Regan, E.C., Wang, D., Jin, C., Bakti Utama, M.I., Gao, B., Wei, X., Zhao, S., Zhao, W., Zhang, Z., Yumigeta, K., *et al.*: Mott and generalized wigner crystal states in wse2/ws2 moiré superlattices. *Nature* **579**(7799), 359–363 (2020)
- [12] Li, H., Li, S., Regan, E.C., Wang, D., Zhao, W., Kahn, S., Yumigeta, K., Blei, M., Taniguchi, T., Watanabe, K., *et al.*: Imaging two-dimensional generalized wigner crystals. *Nature* **597**(7878), 650–654 (2021)
- [13] Zhou, Y., Sung, J., Brutschea, E., Esterlis, I., Wang, Y., Scuri, G., Gelly, R.J., Heo, H., Taniguchi, T., Watanabe, K., *et al.*: Bilayer wigner crystals in a transition metal dichalcogenide heterostructure. *Nature* **595**(7865), 48–52 (2021)
- [14] Andrei, E.Y., MacDonald, A.H.: Graphene bilayers with a twist. *Nature materials* **19**(12), 1265–1275 (2020)
- [15] Yoo, H., Engelke, R., Carr, S., Fang, S., Zhang, K., Cazeaux, P., Sung, S.H., Hovden, R., Tsen, A.W., Taniguchi, T., *et al.*: Atomic and electronic

- reconstruction at the van der waals interface in twisted bilayer graphene. *Nature materials* **18**(5), 448–453 (2019)
- [16] Carr, S., Fang, S., Kaxiras, E.: Electronic-structure methods for twisted moiré layers. *Nature Reviews Materials* **5**(10), 748–763 (2020)
- [17] Xie, H., Luo, X., Ye, G., Ye, Z., Ge, H., Sung, S.H., Rennich, E., Yan, S., Fu, Y., Tian, S., Lei, H., Hovden, R., Sun, K., He, R., Zhao, L.: Twist engineering of the two-dimensional magnetism in double bilayer chromium triiodide homostructures. *Nature Physics* **18**(1), 30–36 (2022)
- [18] Xia, Y., Han, Z., Watanabe, K., Taniguchi, T., Shan, J., Mak, K.F.: Superconductivity in twisted bilayer wse₂. *Nature*, 1–6 (2024)
- [19] Guo, Y., Pack, J., Swann, J., Holtzman, L., Cothrine, M., Watanabe, K., Taniguchi, T., Mandrus, D.G., Barmak, K., Hone, J., *et al.*: Superconductivity in 5.0° twisted bilayer wse₂. *Nature* **637**(8047), 839–845 (2025)
- [20] Maity, I., Maiti, P.K., Krishnamurthy, H., Jain, M.: Reconstruction of moiré lattices in twisted transition metal dichalcogenide bilayers. *Physical Review B* **103**(12), 121102 (2021)
- [21] Dey, A., Chowdhury, S.A., Peña, T., Singh, S., Wu, S.M., Askari, H.: An atomistic insight into moiré’ reconstruction in twisted bilayer graphene beyond the magic angle. *ACS Applied Engineering Materials* **1**(3), 970–982 (2023)
- [22] Choi, Y.W., Choi, H.J.: Strong electron-phonon coupling, electron-hole asymmetry, and nonadiabaticity in magic-angle twisted bilayer graphene. *Physical Review B* **98**(24), 241412 (2018)
- [23] Wu, F., MacDonald, A.H., Martin, I.: Theory of phonon-mediated superconductivity in twisted bilayer graphene. *Physical review letters* **121**(25), 257001 (2018)
- [24] Behnia, K.: Polarized light boosts valleytronics. *Nature nanotechnology* **7**(8), 488–489 (2012)
- [25] Huang, D., Choi, J., Shih, C.-K., Li, X.: Excitons in semiconductor moiré superlattices. *Nature nanotechnology* **17**(3), 227–238 (2022)
- [26] Yu, H., Liu, G.-B., Tang, J., Xu, X., Yao, W.: Moiré excitons: From programmable quantum emitter arrays to spin-orbit-coupled artificial lattices. *Science advances* **3**(11), 1701696 (2017)
- [27] Seyler, K.L., Rivera, P., Yu, H., Wilson, N.P., Ray, E.L., Mandrus, D.G., Yan, J., Yao, W., Xu, X.: Signatures of moiré-trapped valley excitons in mose₂/wse₂ heterobilayers. *Nature* **567**(7746), 66–70 (2019)
- [28] Tran, K., Moody, G., Wu, F., Lu, X., Choi, J., Kim, K., Rai, A., Sanchez, D.A., Quan, J., Singh, A., *et al.*: Evidence for moiré excitons in van der waals heterostructures. *Nature* **567**(7746), 71–75 (2019)

- [29] Jin, C., Regan, E.C., Yan, A., Iqbal Bakti Utama, M., Wang, D., Zhao, S., Qin, Y., Yang, S., Zheng, Z., Shi, S., *et al.*: Observation of moiré excitons in wse2/ws2 heterostructure superlattices. *Nature* **567**(7746), 76–80 (2019)
- [30] Alexeev, E.M., Ruiz-Tijerina, D.A., Danovich, M., Hamer, M.J., Terry, D.J., Nayak, P.K., Ahn, S., Pak, S., Lee, J., Sohn, J.I., *et al.*: Resonantly hybridized excitons in moiré superlattices in van der waals heterostructures. *Nature* **567**(7746), 81–86 (2019)
- [31] Shinokita, K., Miyauchi, Y., Watanabe, K., Taniguchi, T., Matsuda, K.: Resonant coupling of a moiré exciton to a phonon in a wse2/mose2 heterobilayer. *Nano Letters* **21**(14), 5938–5944 (2021)
- [32] Arsenault, E.A., Li, Y., Yang, B., Wang, X., Park, H., Mosconi, E., Ronca, E., Taniguchi, T., Watanabe, K., Gamelin, D., *et al.*: Two-dimensional moiré polaronic electron crystals. *Physical Review Letters* **132**(12), 126501 (2024)
- [33] Campbell, A.J., Brotons-Gisbert, M., Baek, H., Vitale, V., Taniguchi, T., Watanabe, K., Lischner, J., Gerardot, B.D.: Exciton-polarons in the presence of strongly correlated electronic states in a mose2/wse2 moiré superlattice. *npj 2D Materials and Applications* **6**(1), 79 (2022)
- [34] Biswas, S., Zhao, R., Alowa, F., Zacharias, M., Sharifzadeh, S., Coker, D.F., Seferos, D.S., Scholes, G.D.: Exciton polaron formation and hot-carrier relaxation in rigid dion–jacobson-type two-dimensional perovskites. *Nature Materials*, 1–7 (2024)
- [35] Dai, Z., Lian, C., Lafuente-Bartolome, J., Giustino, F.: Excitonic polarons and self-trapped excitons from first-principles exciton-phonon couplings. *Physical Review Letters* **132**(3), 036902 (2024)
- [36] Barré, E., Karni, O., Liu, E., O’Beirne, A.L., Chen, X., Ribeiro, H.B., Yu, L., Kim, B., Watanabe, K., Taniguchi, T., Barmak, K., Lui, C.H., Refaely-Abramson, S., da Jornada, F.H., Heinz, T.F.: Optical absorption of interlayer excitons in transition-metal dichalcogenide heterostructures. *Science* **376**(6591), 406–410 (2022)
- [37] Liu, F., Wu, W., Bai, Y., Chae, S.H., Li, Q., Wang, J., Hone, J., Zhu, X.-Y.: Disassembling 2d van der waals crystals into macroscopic monolayers and reassembling into artificial lattices. *Science* **367**(6480), 903–906 (2020)
- [38] Duncan, C.J., Kaemingk, M., Li, W., Andorf, M., Bartnik, A., Galdi, A., Gordon, M., Pennington, C., Bazarov, I., Zeng, H., *et al.*: Multi-scale time-resolved electron diffraction: A case study in moiré materials. *Ultramicroscopy* **253**, 113771 (2023)
- [39] Qiu, W., Zhang, B., Sun, Y., He, L., Ni, Y.: Atomic reconstruction enabled coupling between interlayer distance and twist in van der waals bilayers. *Extreme Mechanics Letters* **69**, 102159 (2024)

- [40] Durmus, M.A., Sarpkaya, I.: Quantum beats between spin-singlet and spin-triplet interlayer exciton transitions in wse2–mose2 heterobilayers. *Nano Letters* **24**(19), 5767–5773 (2024)
- [41] Kuhlenkamp, C., Kadow, W., Imamoğlu, A., Knap, M.: Chiral pseudospin liquids in moiré heterostructures. *Physical Review X* **14**(2), 021013 (2024)
- [42] Wang, T., Sun, H., Li, X., Zhang, L.: Chiral phonons: Prediction, verification, and application. *Nano Letters* **24**(15), 4311–4318 (2024)
- [43] Biborski, A., Wójcik, P., Zegrodnik, M.: Variational monte carlo approach for the hubbard model applied to twisted bilayer wse 2 at half-filling. *Physical Review B* **109**(12), 125144 (2024)
- [44] Li, W., Duncan, C., Andorf, M., Bartnik, A., Bianco, E., Cultrera, L., Galdi, A., Gordon, M., Kaemingk, M., Pennington, C., et al.: A kiloelectron-volt ultrafast electron micro-diffraction apparatus using low emittance semiconductor photocathodes. *Structural Dynamics* **9**(2) (2022)
- [45] Zaborski, G., Majchrzak, P.E., Lai, S., Johnson, A.C., Saunders, A.P., Zhu, Z., Deng, Y., Lu, D., Hashimoto, M., Shen, Z.-X., Liu, F.: Macroscopic uniform 2D moiré superlattices with controllable angles (2024)
- [46] Carr, S., Massatt, D., Torrisi, S.B., Cazeaux, P., Luskin, M., Kaxiras, E.: Relaxation and domain formation in incommensurate two-dimensional heterostructures. *Physical Review B* **98**(22), 224102 (2018)
- [47] Zhang, K., Tadmor, E.B.: Structural and electron diffraction scaling of twisted graphene bilayers. *Journal of the Mechanics and Physics of Solids* **112**, 225–238 (2018)
- [48] Rosenberger, M.R., Chuang, H.-J., Phillips, M., Oleshko, V.P., McCreary, K.M., Sivaram, S.V., Hellberg, C.S., Jonker, B.T.: Twist angle-dependent atomic reconstruction and moiré patterns in transition metal dichalcogenide heterostructures. *ACS nano* **14**(4), 4550–4558 (2020)
- [49] Sung, S.H., Goh, Y.M., Yoo, H., Engelke, R., Xie, H., Zhang, K., Li, Z., Ye, A., Deotare, P.B., Tadmor, E.B., *et al.*: Torsional periodic lattice distortions and diffraction of twisted 2d materials. *Nature communications* **13**(1), 7826 (2022)
- [50] Sood, A., Haber, J.B., Carlström, J., Peterson, E.A., Barre, E., Georganas, J.D., Reid, A.H., Shen, X., Zajac, M.E., Regan, E.C., et al.: Bidirectional phonon emission in two-dimensional heterostructures triggered by ultrafast charge transfer. *Nature Nanotechnology*, 1–7 (2022)
- [51] Johnson, A.C., Georganas, J.D., Shen, X., Yao, H., Saunders, A.P., Zeng, H.J., Kim, H., Sood, A., Heinz, T.F., Lindenberg, A.M., *et al.*: Hidden phonon highways promote photoinduced interlayer energy transfer in twisted transition metal dichalcogenide heterostructures. *Science Advances* **10**(4), 8819 (2024)

- [52] Britt, T.L., Li, Q., René de Cotret, L.P., Olsen, N., Otto, M., Hassan, S.A., Zacharias, M., Caruso, F., Zhu, X., Siwick, B.J.: Direct view of phonon dynamics in atomically thin mos2. *Nano Letters* **22**(12), 4718–4724 (2022)
- [53] Hu, J., Xiang, Y., Ferrari, B.M., Scalise, E., Vanacore, G.M.: Indirect exciton–phonon dynamics in mos2 revealed by ultrafast electron diffraction. *Advanced Functional Materials* **33**(19), 2206395 (2023)
- [54] Li, C., Scherbakov, A.V., Soubelet, P., Samusev, A.K., Ruppert, C., Balakrishnan, N., Gusev, V.E., Stier, A.V., Finley, J.J., Bayer, M., *et al.*: Coherent phonons in van der waals mose2/wse2 heterobilayers. *Nano Letters* **23**(17), 8186–8193 (2023)
- [55] Nayak, P.K., Horbatenko, Y., Ahn, S., Kim, G., Lee, J.-U., Ma, K.Y., Jang, A.-R., Lim, H., Kim, D., Ryu, S., *et al.*: Probing evolution of twist-angle-dependent interlayer excitons in mose2/wse2 van der waals heterostructures. *ACS nano* **11**(4), 4041–4050 (2017)
- [56] Mannebach, E.M., Nyby, C., Ernst, F., Zhou, Y., Tolsma, J., Li, Y., Sher, M.-J., Tung, I.-C., Zhou, H., Zhang, Q., *et al.*: Dynamic optical tuning of interlayer interactions in the transition metal dichalcogenides. *Nano Letters* **17**(12), 7761–7766 (2017)
- [57] Zeiger, H., Vidal, J., Cheng, T., Ippen, E., Dresselhaus, G., Dresselhaus, M.: Theory for displacive excitation of coherent phonons. *Physical Review B* **45**(2), 768 (1992)
- [58] Naik, M.H., Maity, I., Maiti, P.K., Jain, M.: Kolmogorov–crespi potential for multilayer transition-metal dichalcogenides: capturing structural transformations in moiré superlattices. *The Journal of Physical Chemistry C* **123**(15), 9770–9778 (2019)
- [59] Thompson, A.P., Aktulga, H.M., Berger, R., Bolintineanu, D.S., Brown, W.M., Crozier, P.S., In’t Veld, P.J., Kohlmeyer, A., Moore, S.G., Nguyen, T.D., *et al.*: Lammmps-a flexible simulation tool for particle-based materials modeling at the atomic, meso, and continuum scales. *Computer Physics Communications* **271**, 108171 (2022)
- [60] Naik, S., Naik, M.H., Maity, I., Jain, M.: Twister: Construction and structural relaxation of commensurate moiré superlattices. *Computer Physics Communications* **271**, 108184 (2022)
- [61] Togo, A., Tanaka, I.: First principles phonon calculations in materials science. *Scripta Materialia* **108**, 1–5 (2015)
- [62] González-Manteiga, W., Crujeiras, R.M.: An updated review of goodness-of-fit tests for regression models. *Test* **22**, 361–411 (2013)
- [63] Kolmogorov, A.N., Crespi, V.H.: Registry-dependent interlayer potential for graphitic systems. *Physical Review B* **71**(23), 235415 (2005)

- [64] Wang, K., Huang, B., Tian, M., Ceballos, F., Lin, M.-W., Mahjouri-Samani, M., Boulesbaa, A., Puzos, A.A., Rouleau, C.M., Yoon, M., *et al.*: Interlayer coupling in twisted wse₂/ws₂ bilayer heterostructures revealed by optical spectroscopy. *ACS nano* **10**(7), 6612–6622 (2016)
- [65] Zhu, H., Wang, J., Gong, Z., Kim, Y.D., Hone, J., Zhu, X.-Y.: Interfacial charge transfer circumventing momentum mismatch at two-dimensional van der waals heterojunctions. *Nano letters* **17**(6), 3591–3598 (2017)
- [66] Ji, Z., Hong, H., Zhang, J., Zhang, Q., Huang, W., Cao, T., Qiao, R., Liu, C., Liang, J., Jin, C., *et al.*: Robust stacking-independent ultrafast charge transfer in mos₂/ws₂ bilayers. *ACS nano* **11**(12), 12020–12026 (2017)
- [67] Hu, Z., Wang, H., Wang, L., Wang, H.: A new charge transfer pathway in the mose₂-wse₂ heterostructure under the conditions of b-excitons being resonantly pumped. *Physical Chemistry Chemical Physics* **26**(12), 9424–9431 (2024)
- [68] Wang, J., Ardelean, J., Bai, Y., Steinhoff, A., Florian, M., Jahnke, F., Xu, X., Kira, M., Hone, J., Zhu, X.-Y.: Optical generation of high carrier densities in 2d semiconductor heterobilayers. *Science Advances* **5**(9), 0145 (2019)
- [69] Yan, X., Zhu, L., Zhou, Y., Yiwen, E., Wang, L., Xu, X.: Dielectric property of mos₂ crystal in terahertz and visible regions. *Applied optics* **54**(22), 6732–6736 (2015)
- [70] Gillen, R., Maultzsch, J.: Interlayer excitons in mose₂/wse₂ heterostructures from first principles. *Phys. Rev. B* **97**, 165306 (2018)
- [71] Schmitt, D., Bange, J.P., Bennecke, W., AlMutairi, A., Meneghini, G., Watanabe, K., Taniguchi, T., Steil, D., Luke, D.R., Weitz, R.T., *et al.*: Formation of moiré interlayer excitons in space and time. *Nature* **608**(7923), 499–503 (2022)
- [72] Karni, O., Barré, E., Pareek, V., Georgaras, J.D., Man, M.K., Sahoo, C., Bacon, D.R., Zhu, X., Ribeiro, H.B., O’Beirne, A.L., *et al.*: Structure of the moiré exciton captured by imaging its electron and hole. *Nature* **603**(7900), 247–252 (2022)
- [73] Blundo, E., Tuzi, F., Cianci, S., Cuccu, M., Olkowska-Pucko, K., Kipczak, L., Contestabile, G., Miriametro, A., Felici, M., Pettinari, G., *et al.*: Localisation-to-delocalisation transition of moiré excitons in wse₂/mose₂ heterostructures. *Nature Communications* **15**(1), 1057 (2024)
- [74] Zhong, Y., Zhang, L., Park, J.-H., Cruz, S., Li, L., Guo, L., Kong, J., Wang, E.N.: A unified approach and descriptor for the thermal expansion of two-dimensional transition metal dichalcogenide monolayers. *Science Advances* **8**(46), 3783 (2022)

- [75] Ma, E.Y., Guzelturk, B., Li, G., Cao, L., Shen, Z.-X., Lindenberg, A.M., Heinz, T.F.: Recording interfacial currents on the subnanometer length and femtosecond time scale by terahertz emission. *Science Advances* **5**(2), 0073 (2019)
- [76] Bardeen, J., Shockley, W.: Deformation potentials and mobilities in non-polar crystals. *Physical review* **80**(1), 72 (1950)
- [77] Lu, J.Z., Zhu, Z., Angeli, M., Larson, D.T., Kaxiras, E.: Low-energy moiré phonons in twisted bilayer van der waals heterostructures. *Physical Review B* **106**(14), 144305 (2022)
- [78] Suri, N., Wang, C., Zhang, Y., Xiao, D.: Chiral phonons in moiré superlattices. *Nano letters* **21**(23), 10026–10031 (2021)
- [79] Davies, C., Fennema, F., Tsukamoto, A., Razdolski, I., Kimel, A., Kirilyuk, A.: Phononic switching of magnetization by the ultrafast barnett effect. *Nature*, 1–5 (2024)
- [80] Basini, M., Pancaldi, M., Wehinger, B., Udina, M., Tadano, T., Hoffmann, M., Balatsky, A., Bonetti, S.: Terahertz electric-field driven dynamical multiferroicity in srtio ₃. arXiv preprint arXiv:2210.01690 (2022)
- [81] Luo, J., Lin, T., Zhang, J., Chen, X., Blackert, E.R., Xu, R., Yakobson, B.I., Zhu, H.: Large effective magnetic fields from chiral phonons in rare-earth halides. *Science* **382**(6671), 698–702 (2023)
- [82] Bennett, D.: Theory of polar domains in moiré heterostructures. *Physical Review B* **105**(23), 235445 (2022)
- [83] Schneider, G.F., Calado, V.E., Zandbergen, H., Vandersypen, L.M., Dekker, C.: Wedging transfer of nanostructures. *Nano letters* **10**(5), 1912–1916 (2010)
- [84] Jiang, J.-W.: *Handbook of Stillinger-Weber Potential Parameters for Two-Dimensional Atomic Crystals* (2017)

5 Methods

5.1 UED

Probe electron pulses are generated via photoemission from a Na–K–Sb cathode using 650 nm, 10 ps laser pulses. The probe primary energy is 140 keV. A radiofrequency cavity compresses the electron pulses to <1 ps duration at the sample plane. Sample pumping is performed with 515 nm, 300 fs pulses. The probe spot size on the sample is $3.5 \mu\text{m}$ r.m.s. and the pump spot size $10 \mu\text{m}$ r.m.s.

5.2 Sample preparation

MoSe₂ and WSe₂ monolayers are exfoliated from bulk MoSe₂ and WSe₂ single crystals (HQ graphene) onto 285 nm SiO₂/Si substrate sequentially using a gold tape exfoliation technique [37], forming heterostructures with lateral dimensions of mm scale. The crystal orientations of the monolayers in the heterostructure are aligned with the crystal edges, and further confirmed in electron diffraction and second-harmonic generation. The heterostructures are later transferred onto 10 nm thick, $250 \mu\text{m} \times 250 \mu\text{m}$ Si₃N₄ windows on TEM grids (SiMPore), using a wedging transfer technique with cellulose acetate butyrate (CAB) polymer, and cleaned with ethyl acetate solvent. [83]

5.3 Phonon spectra calculations

We used classical interatomic potentials to describe interactions within individual layers of MoSe₂ and WSe₂ and between the layers. The intralayer interactions in WSe₂ and MoSe₂ were described using a Stillinger-Weber potential [84], while the interlayer interactions are modeled using the Kolmogorov-Crespi (KC) potential [58]. We reproduce an expression for the KC potential here:

$$V(\mathbf{r}_{ij}, \mathbf{n}_i, \mathbf{n}_j) = e^{-\lambda(r_{ij}-z_0)} F(\rho_{ij}) - A \left(\frac{r_{ij}}{z_0} \right)^{-6}, \quad (6)$$

where r_{ij} is the 3D distance between atoms i, j , ρ_{ij} is the 2D in-plane projected distance between atoms i, j , z_0 , λ and A are free parameters and F a parametric function of the in-plane distances alone.

The relaxed atomic positions of our twisted bilayer systems were determined through the implementation of these potentials within the LAMMPS code [59]. The generation of rigidly twisted heterobilayer structures and subsequent relaxations were automated using the TWISTER package [60]. Phonon frequencies and polarization vectors were obtained by diagonalizing the dynamical matrix with a modified version of the PHONOPY code [61].

ROI	WSe ₂ 2°	MoSe ₂ 2°	Sat. 2°	Sum 2°
χ_1^2/N	14	11	4.8	9.9
χ_2^2/N	2.0	0.96	1.4	1.5
χ_3^2/N	1.9	0.89	1.5	1.4
ROI	WSe ₂ 57°	MoSe ₂ 57°	Sat. 57°	Sum 57°
χ_1^2/N	1.3	2.9	1.9	2.0
χ_2^2/N	1.2	0.47	1.1	0.92
χ_3^2/N	1.2	0.43	0.87	0.79

Table 1: Sum of squared residuals normalized by empirical variance and number of data points N for the three dynamical models and two experimental samples. Columns show the individual contributions from each monolayer Bragg peak, satellite peaks and, in the final column, the sum of all three. A value of 1 indicates good fit, significantly greater than 1 that the data is poorly fit and significantly less than 1 that the data is overfit. χ_1^2 is the Debye-Waller-only model, χ_2^2 adds a uniform driving force, χ_3^2 adds a localized force at the moiré exciton trapping sites.

5.4 Goodness of fit

We fit our UED data with a sequence of three nested models. Here we summarize the detailed quantitative description of the three models that can be found the Supplemental Information: model 1 considers only the Debye Waller effect, model 2 assumes a spatially uniform driving force on the lattice and model 3 introduces a spatial modulation to the driving force. To rank the performance of model i , we quantify the lack of fit with a χ_i^2 test statistic:

$$\chi_i^2 = \sum_{n=1}^N \left(\frac{\Delta I}{I}(t_n) - \frac{\Delta \hat{I}_i}{\hat{I}_i}(t_n) \right)^2 / S^2 \quad (7)$$

where I is the measured probe current, \hat{I}_i is the model prediction, S is the empirically estimated r.m.s. uncertainty of the data, and t_n belong to the set of N pump-probe delay times measured. The observed value of these test statistics are shown in Table 1.

The null hypothesis is that the residuals are dependent and normally distributed with variance S^2 , which implies that $\chi_i^2/N = 1$. As described in more detail in the Supplementary Information, the significance of the fit improvement can be quantified with the F_{ij} (Fisher) statistic. We compute the probability that the measured fit improvement \bar{F}_{ij} is an artifact of experimental uncertainty. For the 2 degree sample, we calculate,

$$P(F_{12} > \bar{F}_{12}) = 10^{-16}, \quad (8)$$

$$P(F_{23} > \bar{F}_{23}) = 6 \times 10^{-2}. \quad (9)$$

For the 57 degree sample, we calculate,

$$P(F_{12} > \bar{F}_{12}) = 10^{-11}, \quad (10)$$

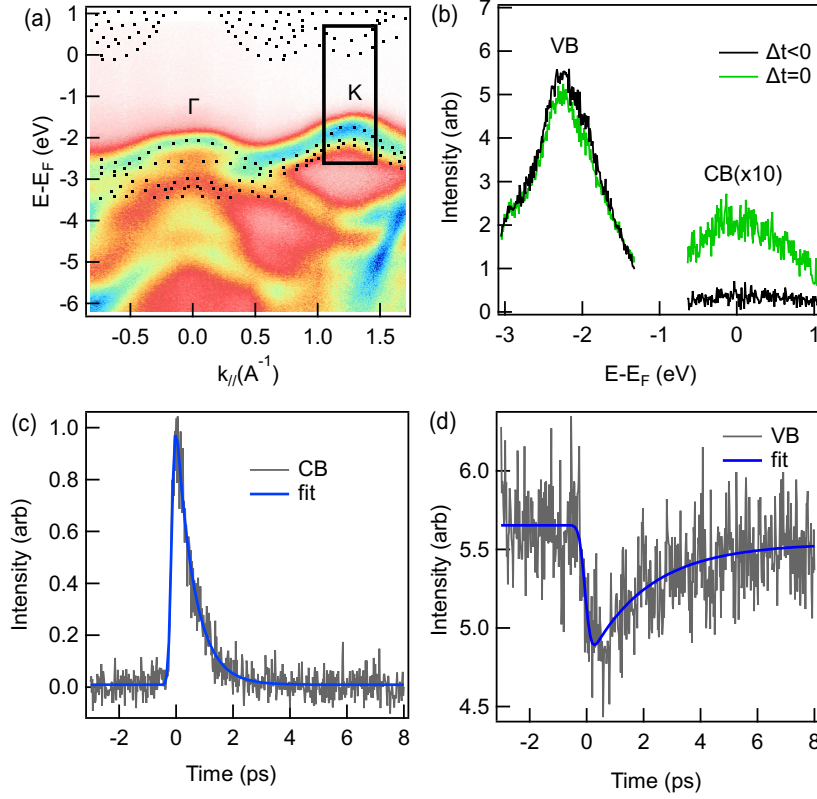
$$P(F_{23} > \bar{F}_{23}) = 2 \times 10^{-3}. \quad (11)$$

These results show that the fit improvement going from model 1 to 2 is unambiguously significant. The fit improvement from model 2 to 3 is suggestive, but reasonable minds may differ on whether the improvement is a statistical artifact.

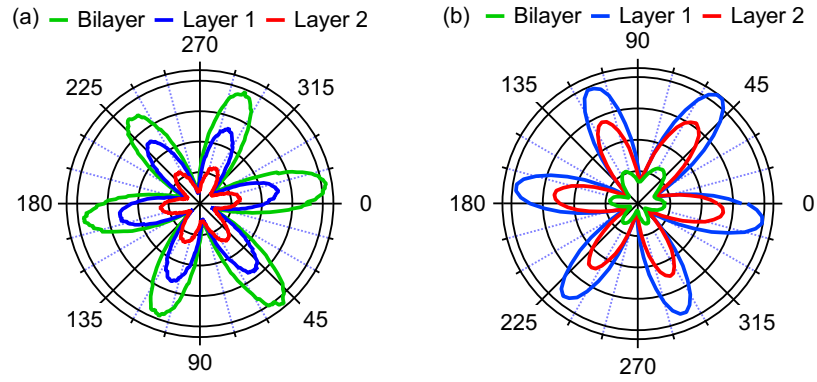
6 Acknowledgements

The UED measurements and instrumentation were supported by the U.S Department of Energy, awards DE-SC0020144 and DE-SC0017631, and U.S. National Science Foundation Grant PHY-1549132, the Center for Bright Beams. Preparation of monolayers and twisted heterobilayers at Stanford is supported by the Defense Advanced Research Projects Agency (DARPA) under Agreement No. HR00112390108. A.M.L. acknowledge support from the U.S. Department of Energy, Office of Science, Basic Energy Sciences, Materials Sciences and Engineering Division, under Contract DE-AC02-76SF00515. The EMPAD detector deployment in this experiment was funded in part by the Kavli Institute at Cornell. The authors are profoundly grateful to Prof. Xiaoyang Zhu for his generous support and guidance in facilitating the trARPES measurements conducted using the setup in his lab at Columbia University.

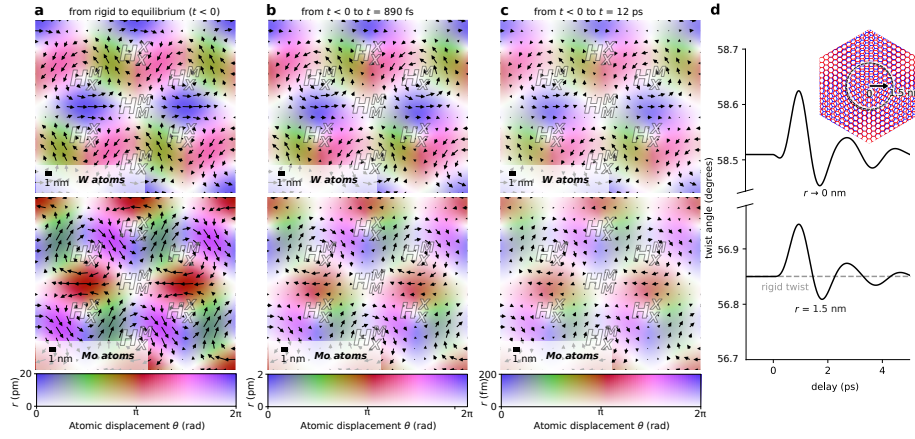
7 Extended Data



Extended Data 1: Time- and angle-resolved photoemission spectra (trARPES) of a 3° MoSe₂/WSe₂ heterostructure. (a) Static ARPES band structure. The dot lines are theoretical prediction reproduced from [70]. The box highlights the region around K point at which the electrons and holes are monitored. (b) Electron energy distribution curve (EDC) near valence band (VB) and the conduction band (CB) edges at K point, before and after the pump excitation. (c)(d) Time-dependent CB and VB ARPES signals showing the evolution of electron and hole populations at the K point. Solid blue lines correspond to fit to exponential decay convoluted with the time resolution of ~ 120 fs. The CB electron dynamics is best fit to a single exponential decay with time constant of 630 fs. The population of the VB holes is best fit to a double exponential decay with time constants of 2 ps and 97 ps. The trARPES is performed with a 2.34 eV pump with a power density of ~ 1.2 mJ/cm², and 21.7 eV EUV probe beam, under room temperature.



Extended Data 2: Second harmonic generation (SHG) polarization scan on the 2° (a) and 57° (b) WSe₂/MoSe₂ heterobilayers for UED measurements. The alignment of crystal axes in the two layers are determined by the constructive and destructive interference. The SHG signals were excited using a 1030 nm femtosecond laser with < 200 fs pulse duration under room temperature, and captured by an EM CCD detector.



Extended Data 3: Twisting of the 57° $\text{WSe}_2/\text{MoSe}_2$ lattice versus time, extracted from our dynamical model fitted to UED experimental data. (a) At equilibrium, atoms are displaced from sites of the unphysical, rigidly rotated lattice by vdW forces. Color map indicates local atomic displacement in polar coordinates: hue shows displacement direction (θ) in radians, saturation displacement magnitude (r) in picometers. (b) Snapshot of the transverse displacement of atoms from equilibrium at 890 fs after photoexcitation, dominated by torsion about the H_X^M stacking domain center. (c) Snapshot at 12 ps following photoexcitation, i.e., after the decay of the oscillatory transient. (d) Fitted atomic displacement as a function of radial distance from the vortex center, expressed as a twist angle.

8 Supplementary Information

Contents

- 8.1 Linearized dynamical model
- 8.2 Equivalence of driving force with the DECP formalism
- 8.3 Kinematic diffraction analysis
- 8.4 Goodness of fit
- 8.5 Toy Lagrangian

8.1 Linearized dynamical model

This subsection derives Eqs. 1-3 and 6 of the main text, which together comprise our model of the lattice dynamics in response to pump excitation. Starting with the time-independent terms on the right-hand-side of main-text Eq. 1, we can define a stiffness tensor in terms of the non-perturbative Lagrangian L ,

$$C_{ijkl} := \frac{\partial^2 L}{\partial x_{ij} \partial x_{kl}}. \quad (\text{S1})$$

Then a linearized lattice Lagrangian L_0 can be defined near equilibrium,

$$L_0 = \frac{1}{2} \sum_{ij} m_j \dot{x}_{ij}^2 - \frac{1}{2} \sum_{ijkl} C_{ijkl} x_{ij} x_{kl}. \quad (\text{S2})$$

The indices ij can be flattened to a single index I over all the real-valued degrees of freedom in the problem. Making the change of variables to mass-weighted degrees of freedom $y_I = x_I \sqrt{\frac{m_I}{\langle m \rangle}}$:

$$L_0 = \langle m \rangle \frac{1}{2} \sum_I \dot{y}_I^2 - \frac{1}{2} \langle m \rangle \sum_{IJ} \frac{C_{IJ}}{\sqrt{m_I m_J}} y_I y_J. \quad (\text{S3})$$

From the properties of the partial derivative, the matrix $A_{IJ} := C_{IJ}/\sqrt{m_I m_J}$ is real and symmetric and can therefore be diagonalized with eigenvalues c_i by the orthogonal change of basis matrix U_{iI} . Transformed degrees of freedom η_i (normal mode amplitudes) can then be defined:

$$\eta_i = \sum_I U_{iI} y_I. \quad (\text{S4})$$

The system decouples in these degrees of freedom:

$$L_0 = \frac{1}{2} \langle m \rangle \sum_i \dot{\eta}_i^2 - \frac{1}{2} \langle m \rangle \sum_i c_i \eta_i^2. \quad (\text{S5})$$

The Euler-Lagrange equations are thus,

$$\ddot{\eta}_i = -c_i \eta_i, \quad (\text{S6})$$

with well known harmonic solutions, such that the normal mode frequencies are $\omega_i = \sqrt{c_i}$. Adding a damping term gives,

$$\ddot{\eta}_i = -2\omega_i\dot{\eta}_i - \omega_i^2\eta_i. \quad (\text{S7})$$

We can now substitute back the definition of η_i in terms of x_I to obtain,

$$\sum_I U_{iI} \sqrt{\frac{m_I}{\langle m \rangle}} \ddot{x}_I = - \sum_I U_{iI} \sqrt{\frac{m_I}{\langle m \rangle}} (2\omega_i \dot{x}_I + \omega_i^2 x_I). \quad (\text{S8})$$

Multiplying through U^{-1} ,

$$\ddot{x}_J = - \sum_{iI} U_{iJ} U_{iI} \sqrt{\frac{m_I}{m_J}} (2\omega_i \dot{x}_I + \omega_i^2 x_I). \quad (\text{S9})$$

Finally, unravelling the indices IJ and relabelling dummy indices,

$$\ddot{x}_{ij} = - \sum_{k\ell q} U_{kij} U_{k\ell q} \sqrt{\frac{m_\ell}{m_i}} (2\omega_k \dot{x}_{\ell q} + \omega_k^2 x_{\ell q}). \quad (\text{S10})$$

It remains to justify the inclusion of the driving term in Eq. 1. The microscopic origin of the force perturbing the lattice in our interpretation is the Coulomb attraction of layer-separated charges. We proceeded by writing an expression for the macroscopic energy stored in the system due to charge separation, as a function of the layer separation z . We then derive a macroscopic out-of-plane pressure from this stored energy. The driving force on each atom in our model is then simply this macroscopic pressure divided by the surface density of atoms. The energy per unit area \mathcal{E} stored in a parallel plate capacitor is given by,

$$\mathcal{E} = \frac{\rho^2 z}{2\epsilon}, \quad (\text{S11})$$

where ρ is charge per unit area. Now taking the derivative with respect to z , we obtain the force per unit area P_C ,

$$P_C = - \frac{\partial \mathcal{E}}{\partial z} = - \frac{\rho^2}{2\epsilon}. \quad (\text{S12})$$

Main-text Eq. 6 follows after rewriting in terms of the number density $n := \rho/e$. Charges recombine over a characteristic timescale τ , and so the capacitive pressure decays with time as,

$$P_C(t) = - \frac{\rho_0^2 e^{-2t/\tau}}{2\epsilon}, \quad (\text{S13})$$

with ρ_0 the peak photo-excited charge density. On the same timescale, lattice heating applies an outward pressure rising to an asymptotic value of P_0 to give an expression for the total pressure over the delay times of interest:

$$P(t) = (1 - e^{-t/\tau})P_0 - \frac{\rho_0^2 e^{-2t/\tau}}{2\epsilon}, \quad (\text{S14})$$

which is of the form of main-text Eq. 3.

8.2 Equivalence of driving force with the DECP formalism

According to the theory of the displacive excitation of coherent phonons (DECP), ultrafast lattice motion is caused by a change to the coordinate of the potential minima $\bar{x}_{ij}(t)$, where i indexes the atom and j the vector component of the displacement from the old equilibrium. In this formalism, Eq. (1) of the main text can be written,

$$\ddot{x}_{ij} = - \sum_{k\ell q} U_{kij} U_{k\ell q} \sqrt{\frac{m_\ell}{m_i}} (2\omega_k \dot{x}_{\ell q} + \omega_k^2 (x_{\ell q} - \bar{x}_{\ell q}(t))). \quad (\text{S15})$$

The equivalence of Eq. (S15) to main-text Eq. (1) follows on making the substitution:

$$\bar{x}_{\ell q}(t) := \sum_{rst} U_{r\ell q} U_{rst} \sqrt{\frac{m_s}{m_\ell}} \omega_r^{-2} F_{st}(t), \quad (\text{S16})$$

with $F_{ij}(t)$ the driving force from main-text Eq. (1). Equation (S15) then becomes,

$$\ddot{x}_{ij} = - \sum_{k\ell q} U_{kij} U_{k\ell q} \sqrt{\frac{m_\ell}{m_i}} \left(2\omega_k \dot{x}_{\ell q} + \omega_k^2 \left(x_{\ell q} - \sum_{rst} U_{rst} U_{r\ell q} \sqrt{\frac{m_s}{m_\ell}} \omega_r^{-2} F_{st}(t) \right) \right), \quad (\text{S17})$$

which after expanding the brackets includes a term,

$$\begin{aligned} & \sum_{k\ell qrst} U_{kij} U_{k\ell q} U_{r\ell q} U_{rst} \sqrt{\frac{m_s}{m_i}} \frac{\omega_k^2}{\omega_r^2} F_{st}(t) \\ &= \sum_{krst} U_{kij} \delta_{kr} U_{rst} \sqrt{\frac{m_s}{m_i}} \frac{\omega_k^2}{\omega_r^2} F_{st}(t) \\ &= \sum_{kst} U_{kij} U_{kst} \sqrt{\frac{m_s}{m_i}} F_{st}(t) \\ &= \sum_{st} \delta_{is} \delta_{jt} \sqrt{\frac{m_s}{m_i}} F_{st}(t) \\ &= F_{ij}(t), \end{aligned} \quad (\text{S18})$$

where δ is the Kronecker delta symbol. In taking these steps, use is made of the identities that follow from the orthonormality of the normal modes of oscillation, namely:

$$\sum_{\ell q} U_{k\ell q} U_{r\ell q} = \delta_{kr}, \quad (\text{S19})$$

and,

$$\sum_k U_{kij} U_{kst} = \delta_{is} \delta_{jt}. \quad (\text{S20})$$

8.3 Kinematic diffraction analysis

This subsection derives the expected diffraction signal from the moiré lattice. Assume an electron plane wave incident on the sample with wave vector \mathbf{k}_0 . Letting \mathbf{r} be the position on the detector measured with respect to the sample, the solution to the Schroedinger equation in the first Born approximation is,

$$\psi(\mathbf{r}) = e^{i\mathbf{k}_0 \cdot \mathbf{r}} + \frac{2\pi m e}{\hbar^2} \frac{e^{ik_0 r}}{r} \hat{V}(k\hat{\mathbf{r}} - \mathbf{k}_0), \quad (\text{S21})$$

where \hat{V} is the Fourier transform of the sample potential. Our experiment represents the special case in which \mathbf{k}_0 is normal to the bilayer and $\mathbf{q} := k\mathbf{r} - \mathbf{k}_0$ is parallel. The potential \hat{V} can be decomposed into the sum of six monolayers \hat{V}_i ,

$$\hat{V} = \sum_{i=1}^N \hat{V}_i. \quad (\text{S22})$$

The \hat{V}_i in turn can be decomposed into a product of the the Fourier transform of the potential due to an individual atom \hat{G}_i and the Fourier transform of the crystal lattice \hat{F}_i , i.e., letting \mathbf{r}_{ij} be the position of the j th atom belonging to the i th monolayer,

$$\hat{F}_i(\mathbf{q}) = \int_{-\infty}^{\infty} \int_{-\infty}^{\infty} \int_{-\infty}^{\infty} \sum_j \delta(\mathbf{r} - \mathbf{r}_{ij}) e^{-i\mathbf{q} \cdot \mathbf{r}} dx dy dz, \quad (\text{S23})$$

$$\hat{V}_i = (\hat{G}_i \hat{F}_i) * \hat{\Omega}. \quad (\text{S24})$$

The indicator function $\Omega(\mathbf{r})$ is unity if \mathbf{r} lies within the finite bounds of the crystal and vanishes otherwise. Neglecting for the moment the displacement due to moiré reconstruction, the \hat{F}_i are all equal up to rotation and translation. Let us therefore define a fiducial \hat{F} as follows:

$$\hat{F}(\mathbf{q}) = \sum_{n=-\infty}^{\infty} \sum_{m=-\infty}^{\infty} \delta\left(\mathbf{q} - \frac{2\pi n}{a} \hat{\mathbf{x}} - \frac{2\pi m}{\sqrt{3}a} \hat{\mathbf{y}} - \frac{4\pi m}{\sqrt{3}a} \hat{\mathbf{y}}\right), \quad (\text{S25})$$

where a is the transverse lattice constant for WSe_2 . Letting R and \mathbf{d} be respectively the rotation matrix and translation vector,

$$R = \begin{pmatrix} \cos(\theta/2) & -\sin(\theta/2) \\ \sin(\theta/2) & \cos(\theta/2) \\ & & 1 \end{pmatrix}, \quad \mathbf{d} = \begin{pmatrix} a/2 \\ a/\sqrt{12} \\ 0 \end{pmatrix}, \quad (\text{S26})$$

we then obtain, when restricted to \mathbf{q} parallel to the bilayer surface, for the R -type stacking:

$$\hat{F}_0(\mathbf{q}) = e^{i(R^{-1}\mathbf{q})\cdot\mathbf{d}}\hat{F}(R\mathbf{q}), \quad (\text{S27})$$

$$\hat{F}_1(\mathbf{q}) = \hat{F}(R\mathbf{q}), \quad (\text{S28})$$

$$\hat{F}_2(\mathbf{q}) = e^{i(R^{-1}\mathbf{q})\cdot\mathbf{d}}\hat{F}(R\mathbf{q}), \quad (\text{S29})$$

$$\hat{F}_3(\mathbf{q}) = e^{i(R\mathbf{q})\cdot\mathbf{d}}\hat{F}(R^{-1}\mathbf{q}), \quad (\text{S30})$$

$$\hat{F}_4(\mathbf{q}) = \hat{F}(R^{-1}\mathbf{q}), \quad (\text{S31})$$

$$\hat{F}_5(\mathbf{q}) = e^{i(R\mathbf{q})\cdot\mathbf{d}}\hat{F}(R^{-1}\mathbf{q}). \quad (\text{S32})$$

The case of H type stacking is obtained by rotating MoSe_2 by $\pi/3$. Although each monolayer is invariant under a $\pi/3$ rotation, the stacked structure is only invariant under a $2\pi/3$ rotation. The effect of a $\pi/3$ rotation is instead equivalent to a permutation, i.e., chalcogenide atoms go to the locations previously occupied by metal atoms and vice versa. Hence, for H -type stacking:

$$\hat{F}_0(\mathbf{q}) = \hat{F}(R\mathbf{q}) \quad (\text{S33})$$

$$\hat{F}_1(\mathbf{q}) = e^{i(R^{-1}\mathbf{q})\cdot\mathbf{d}}\hat{F}(R\mathbf{q}) \quad (\text{S34})$$

$$\hat{F}_2(\mathbf{q}) = \hat{F}(R\mathbf{q}) \quad (\text{S35})$$

$$\hat{F}_3(\mathbf{q}) = e^{i(R\mathbf{q})\cdot\mathbf{d}}\hat{F}(R^{-1}\mathbf{q}) \quad (\text{S36})$$

$$\hat{F}_4(\mathbf{q}) = \hat{F}(R^{-1}\mathbf{q}) \quad (\text{S37})$$

$$\hat{F}_5(\mathbf{q}) = e^{i(R\mathbf{q})\cdot\mathbf{d}}\hat{F}(R^{-1}\mathbf{q}). \quad (\text{S38})$$

Now we take into consideration moiré reconstruction, denoted \hat{F}'_i . We consider only the longest wavelength features of the torsional motion and make the simplifying assumption, vindicated by numerical simulations, that the torsion is concentric across all six layers. We make no assumptions about the amplitude of the motion: let A_i be the amplitude for the i th layer. The displacement field $\mathbf{u}_i(\mathbf{r})$ is described by three superlattice wavevectors \mathbf{K}_i ,

$$\mathbf{K}_0 := \frac{4\pi\theta}{\sqrt{3}a}\hat{\mathbf{x}}, \quad (\text{S39})$$

$$\mathbf{K}_1 := -\frac{2\pi\theta}{\sqrt{3}a}\hat{\mathbf{x}} + \frac{2\pi\theta}{a}\hat{\mathbf{y}}, \quad (\text{S40})$$

$$\mathbf{K}_2 := -\mathbf{K}_0 - \mathbf{K}_1, \quad (\text{S41})$$

with,

$$\mathbf{u}_i = -A_i\nabla \times \sum_{j=0}^2 \cos(\mathbf{K}_j \cdot \mathbf{r})\hat{\mathbf{z}}. \quad (\text{S42})$$

Expressing the displacement field in terms of the curl of another function makes it simpler to compute the following compact expression for $\mathbf{q} \cdot \mathbf{u}_i$,

$$\mathbf{q} \cdot \mathbf{u}_i = A_i \sum_{j=0}^2 [\mathbf{K}_j \times \mathbf{q}]_z \sin(\mathbf{K}_j \cdot \mathbf{r}), \quad (\text{S43})$$

where we use the shorthand notation for the operations on vectors \mathbf{v} , \mathbf{w} ,

$$[\mathbf{v} \times \mathbf{w}]_z := v_x w_y - v_y w_x. \quad (\text{S44})$$

From Eq. (S23), and performing the integral,

$$\hat{F}'_i(\mathbf{q}) = \sum_j e^{i\mathbf{q} \cdot (\mathbf{r}_{ij} + \mathbf{u}_i)}. \quad (\text{S45})$$

We now make use of the Jacobi-Anger expansion (a mathematical identity),

$$e^{iA \sin(\phi)} = \sum_{n=-\infty}^{\infty} J_n(A) e^{in\phi}, \quad (\text{S46})$$

where J_n is the n th bessel function. Here the index n gives rise to sidebands in the diffraction pattern: to simplify the analysis we truncated $n \leq 1$ and expand the bessel function to leading order, so that Eq. (S46) simplifies to:

$$e^{iA \sin(\phi)} \approx 1 + \frac{A}{2} (e^{i\phi} - e^{-i\phi}). \quad (\text{S47})$$

Substituting this approximation into Eq. (S45) and retaining terms at most linear in the displacement amplitudes A_i ,

$$\hat{F}'_i(\mathbf{q}) = \sum_j \left\{ e^{i\mathbf{q} \cdot \mathbf{r}_{ij}} + \frac{A_i}{2} \sum_{k=0}^2 [\mathbf{K}_k \times \mathbf{q}]_z \left(e^{i(\mathbf{q} + \mathbf{K}_k) \cdot \mathbf{r}_{ij}} - e^{i(\mathbf{q} - \mathbf{K}_k) \cdot \mathbf{r}_{ij}} \right) \right\}, \quad (\text{S48})$$

Recognizing that each of the terms in Eq. (S48) is related to the rigid lattice by a translation in reciprocal space $\mathbf{q} \mapsto \mathbf{q} \pm \mathbf{K}_i$, we obtain,

$$\hat{F}'_i(\mathbf{q}) = \hat{F}_i(\mathbf{q}) + \frac{A_i}{2} \sum_{k=0}^2 [\mathbf{K}_k \times \mathbf{q}]_z \left(\hat{F}_i(\mathbf{q} + \mathbf{K}_k) - \hat{F}_i(\mathbf{q} - \mathbf{K}_k) \right). \quad (\text{S49})$$

We now evaluate \hat{F} at peaks within the experimental ROI centered on the reciprocal space vector:

$$\mathbf{q}_0 := \frac{4\pi}{a} \hat{\mathbf{x}}. \quad (\text{S50})$$

The two Bragg peaks \mathbf{q}_1 , \mathbf{q}_2 are located at,

$$\mathbf{q}_1 = R\mathbf{q}_0, \quad \mathbf{q}_2 = R^{-1}\mathbf{q}_0. \quad (\text{S51})$$

The phase prefactors arising from the displacement between metal and chalcogenide layers are thus,

$$\exp \{i(R^{\pm 1} \mathbf{q}_{1,2}) \cdot \mathbf{d}\} = 1. \quad (\text{S52})$$

It thus follows that,

$$\hat{V}(\mathbf{q}_1) = (\hat{G}_1 + \hat{G}_2 + \hat{G}_3) \mathcal{N}, \quad (\text{S53})$$

$$\hat{V}(\mathbf{q}_2) = (\hat{G}_4 + \hat{G}_5 + \hat{G}_6) \mathcal{N}, \quad (\text{S54})$$

where \mathcal{N} is the total number of unit cells contained in the volume of the crystal, and arises from the convolution with the indicator function Ω in Eq. (S24).

Turning to the satellite peaks $\mathbf{q}_3, \mathbf{q}_4$, in the small angle approximation of the rotation matrix R ,

$$\mathbf{q}_1 = \mathbf{q}_0 + \frac{2\pi\theta}{a} \hat{\mathbf{y}}, \quad \mathbf{q}_2 = \mathbf{q}_0 - \frac{2\pi\theta}{a} \hat{\mathbf{y}}. \quad (\text{S55})$$

Comparing with the superlattice wavevectors, inspection shows that,

$$\mathbf{q}_1 = \mathbf{q}_0 + \mathbf{K}_1 - \frac{1}{2}\mathbf{K}_0, \quad \mathbf{q}_2 = \mathbf{q}_0 - \mathbf{K}_1 + \frac{1}{2}\mathbf{K}_0. \quad (\text{S56})$$

We thus have,

$$\mathbf{q}_3 = \mathbf{q}_1 + \mathbf{K}_2 = \mathbf{q}_2 + \mathbf{K}_1 = \mathbf{q}_0 - \frac{1}{2}\mathbf{K}_0 \quad (\text{S57})$$

$$\mathbf{q}_4 = \mathbf{q}_1 - \mathbf{K}_1 = \mathbf{q}_2 - \mathbf{K}_2 = \mathbf{q}_0 + \frac{1}{2}\mathbf{K}_0, \quad (\text{S58})$$

and therefore, to linear order in the twist angle θ ,

$$\hat{V}(\mathbf{q}_3) = \frac{8\pi^2\theta}{\sqrt{3}a^2} (A_1\hat{G}_1 + A_2\hat{G}_2 + A_3\hat{G}_3 - A_4\hat{G}_4 - A_5\hat{G}_5 - A_6\hat{G}_6) \mathcal{N}, \quad (\text{S59})$$

$$\hat{V}(\mathbf{q}_4) = -\frac{8\pi^2\theta}{\sqrt{3}a^2} (A_1\hat{G}_1 + A_2\hat{G}_2 + A_3\hat{G}_3 - A_4\hat{G}_4 - A_5\hat{G}_5 - A_6\hat{G}_6) \mathcal{N}. \quad (\text{S60})$$

Inspection of Eq. (S59) shows that, taking the magnitudes of the A_i as given, \hat{V} is maximum when the amplitudes corresponding to WSe₂, i.e., A_1, A_2, A_3 , are opposite in sign to those corresponding to MoSe₂, i.e., A_4, A_5, A_6 .

8.4 Goodness of fit

This section provides a more detailed discussion of the statistical significance of the fits to the UED data shown in main-text Fig. 2. The experimental observables are the relative change in beam current $\Delta I_i(t)/I_i$ with i indexing the three reciprocal space regions of interest (ROI) indicated in Fig. 1. These ROI are 1. the WSe₂ Bragg peak, 2. the MoSe₂ Bragg peak and 3. the sum of the two satellite peaks. We fit these data with a sequence of three *nested* models,

nested meaning that if $i > j$ then model i contains all parameters present in model j . To avoid ambiguity, we denote the model predictions $\Delta \hat{I}_{ij}$ where the index i denotes the ROI and the index j denotes the nest-level of the model. The common element of all three models is an exponential envelope $D_{ij}(t)$, which is the UED response typical of electron-lattice thermal equilibration, defined for ROIs 1 and 2 to be:

$$D_{ij}(t) := \left(A_{ij} \left[e^{(t_0-t)/\tau_{ij}} H(t-t_0) + H(t_0-t) \right] + 1 - A_{ij} \right) * e^{-0.5t/\sigma^2}, \quad (\text{S61})$$

where A_{ij} is the amplitude of the modulation in ROI i , t_0 is the arrival time of the laser, τ_{ij} is a relaxation time, and σ is the r.m.s. time resolution of the instrument. The satellite envelope $D_{3,i}$ is the weighted average of monolayer contributions:

$$D_{3,i} = p_1 D_{1,i} + p_2 D_{2,i} + p_3 \sqrt{D_{1,i} D_{2,i}}, \quad (\text{S62})$$

with p given by the ratio of monolayer structure amplitudes, F_{MX_2} :

$$p_1 = \frac{F_{\text{WSe}_2}^2}{F_{\text{WSe}_2}^2 + F_{\text{MoSe}_2}^2 + 2F_{\text{WSe}_2} F_{\text{MoSe}_2}}, \quad (\text{S63})$$

$$p_2 = \frac{F_{\text{MoSe}_2}^2}{F_{\text{WSe}_2}^2 + F_{\text{MoSe}_2}^2 + 2F_{\text{WSe}_2} F_{\text{MoSe}_2}}, \quad (\text{S64})$$

$$p_3 = 1 - p_1 - p_2. \quad (\text{S65})$$

Models 2 and 3 involve an extra factor we denote Ψ_{ij} that cannot be expressed in closed form, and is obtained by first solving Eq. (1) numerically and then simulating the diffraction pattern in the zero temperature, kinematic limit. We perform these steps with a custom Python code. The function Ψ_{ij} is normalized to the static diffraction intensity such that $\Psi_{i,j}(t < t_0) := 1$ for all ROIs. In model 1, there are two additional fitting parameters a_2, b_2 that describe the spatially-uniform driving force, according to the expression in Eq. (3). The most complex model includes an addition spatially-dependent driving force F_ℓ ,

$$F_\ell(\mathbf{r}) = c_3 \sum_n \exp \left\{ -\frac{1}{2c_4^2} \|\mathbf{r} - \mathbf{x}_n\|^2 \right\}, \quad (\text{S66})$$

where \mathbf{x}_n are the periodic minima in the moiré potential and the fitting parameters c_3, c_4 quantify the strength and localisation of the force. The predictions of the three models are then,

$$\Delta \hat{I}_{i,1}(t) = \hat{I}_{i,1} D_{i,1}(t), \quad (\text{S67})$$

$$\Delta \hat{I}_{i,2}(t) = \hat{I}_{i,2} D_{i,2}(t) \Psi_{i,2}(t; a_2, b_2), \quad (\text{S68})$$

$$\Delta \hat{I}_{i,3}(t) = \hat{I}_{i,3} D_{i,3}(t) \Psi_{i,3}(t; a_3, b_3, c_3), \quad (\text{S69})$$

where \hat{I}_{ij} is the best fit according to model j of the static beam intensity in ROI i , i.e., at times $t < t_0$. The number of fit parameters ν_i for the i th model are therefore $\nu_1 = 8$, $\nu_2 = 10$ and $\nu_3 = 11$.

ROI	WSe ₂ 2°	MoSe ₂ 2°	Sat. 2°	Sum 2°
χ_1^2/N	14	11	4.8	9.9
χ_2^2/N	2.0	0.96	1.4	1.5
χ_3^2/N	1.9	0.89	1.5	1.4
ROI	WSe ₂ 57°	MoSe ₂ 57°	Sat. 57°	Sum 57°
χ_1^2/N	1.3	2.9	1.9	2.0
χ_2^2/N	1.2	0.47	1.1	0.92
χ_3^2/N	1.2	0.43	0.87	0.79

Table S1: Sum of squared residuals normalized by empirical variance and number of data points N for the three dynamical models and two experimental samples. Columns show the individual contributions from each monolayer Bragg peak, satellite peaks and, in the final column, the sum of all three. A value of 1 indicates good fit, significantly greater than 1 that the data is poorly fit and significantly less than 1 that the data is overfit. More detail can be found in the Supplemental Information

To rank the performance of model i , we quantify the lack of fit with a χ_i^2 test statistic:

$$\chi_i^2 = \sum_{n=1}^N \left(\frac{\Delta I}{I}(t_n) - \frac{\Delta \hat{I}_i}{\hat{I}_i}(t_n) \right)^2 / S^2 \quad (\text{S70})$$

where S is the empirically estimated r.m.s. uncertainty of the data, and t_n belong to the set of N pump-probe delay times measured. In a previous publication, we present data analysis verifying that the dominant contribution to experimental uncertainty is Poisson noise, i.e., uncertainty arising from the fact that there are only a finite number of scattering events recorded [38]. The observed value of these test statistics are shown in Table S1.

The null hypothesis is that the residuals are dependent and normally distributed with variance S^2 , which implies that $\chi_i^2/N = 1$.

The nesting of the models guarantees that $\chi_3^2 < \chi_2^2 < \chi_1^2$. The significance of the fit improvement can be quantified with the F_{ij} (Fisher) statistic, defined for $j > i$,

$$F_{ij} := \frac{\chi_i^2 - \chi_j^2}{\chi_j^2} \frac{N - \nu_j}{\nu_j - \nu_i}. \quad (\text{S71})$$

The larger the value of F_{ij} , the greater improvement model j makes over model i . If the fit residuals are normally distributed with variance S^2 (i.e., both models i and j fit the data well) then the F statistic follows the F probability distribution. We can then compute the probability that the measured fit improvement \bar{F}_{ij} is an artifact of experimental uncertainty. For the 2 degree sample, we calculate,

$$P(F_{12} > \bar{F}_{12}) = 10^{-16}, \quad (\text{S72})$$

$$P(F_{23} > \bar{F}_{23}) = 6 \times 10^{-2}. \quad (\text{S73})$$

For the 57 degree sample, we calculate,

$$P(F_{12} > \bar{F}_{12}) = 10^{-11}, \quad (\text{S74})$$

$$P(F_{23} > \bar{F}_{23}) = 2 \times 10^{-3}. \quad (\text{S75})$$

These results show that the fit improvement going from model 1 to 2 is unambiguously significant. The fit improvement from model 2 to 3 is suggestive, but reasonable minds may differ on whether the improvement is a statistical artifact.

8.5 Toy Lagrangian

To better elucidate the mechanism that couples in-plane and out-of-plane lattice motion, it is helpful to refer to a toy model that retains only two mesoscopic degrees of freedom: the twist angle θ about the vortex center in the moiré supercell and the spatially averaged interlayer separation z . The quadratic Lagrangian L in these variables is,

$$L = \frac{1}{2}I\dot{\theta}^2 + \frac{1}{2}M\dot{z}^2 - \frac{1}{2}I\omega_{\parallel}^2(\theta - \theta_0)^2 - \frac{1}{2}M\omega_{\perp}^2(z - z_0)^2 - \frac{1}{2}V(\theta - \theta_{\max})^2 + V\theta\theta_{\max}\lambda(z - z_0). \quad (\text{S76})$$

Here I and M are the moment of inertia and the mass per moiré supercell respectively, ω_{\parallel} quantifies the strength of the purely intralayer elastic restoring force, ω_{\perp} is the frequency of the purely out-of-plane breathing motion that would be present at zero-twist angle, and V is the vdW energy that gives rise to the PLD. As a consequence of the fact that vdW forces are much weaker than in-plane bonds, $\omega_{\parallel} > \omega_{\perp}$ except at twist angles much smaller than our samples. The intralayer elastic equilibrium of the lattice is at the rigid twist angle θ_0 , whereas the interlayer vdW equilibrium is θ_{\max} .